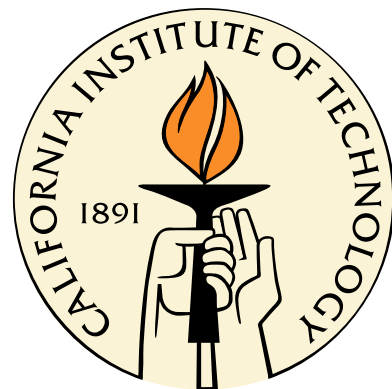


The Radio Variability of Gamma-Ray Blazars

Thesis by
Joseph Lee Richards

In Partial Fulfillment of the Requirements
for the Degree of
Doctor of Philosophy



California Institute of Technology
Pasadena, California

2012
(Defended October 11, 2011)

© 2012

Joseph Lee Richards

All Rights Reserved

Acknowledgments

I must of course thank my family for their love, support, and so much more throughout this research. Thanks to my wife, Elina, for introducing me to astronomy, for providing the impetus to return to graduate school, and for tolerating several extra years in sunny California while I finished up. Our children, Jesse and Wendy, have provided a constant reminder that there are always things more important than research. To my parents, I owe thanks for teaching me the value of education and hard work, and for making any of this possible.

I am extremely grateful to my fellow student, Walter Max-Moerbeck, who performed far more than his share of observing, and for his patiently helping a physics student learn some astronomy. Thanks also to Matthew Stevenson, who, among many things, kept the monitoring program going at a critical juncture. Postdoctoral scholar Vaso Pavlidou has provided uncountable theoretical discussions as well as reliable advice and valuable CPU cycles, for which I am grateful. Thanks are also due to Tim Pearson for scientific guidance, always-thoughtful criticism, and technical support. Martin Shepherd's tireless dedication to precision and completeness has been inspirational, and any understanding I have of spherical trigonometry is owed to him. Erik Leitch helpfully laid out the fundamentals of calibrating 40 m data in his thesis, and his assistance debugging and extending his CMBPROG software was a great help. I would also like to thank Keith Grainge for many discussions about calibration and data filtering and for his unflappable good cheer. Mark Birkinshaw also provided very helpful suggestions on this topic, as well as fascinating stories about the 40 m. Many thanks to Dave Meier for the privilege of reading a manuscript of his forthcoming textbook on AGN physics. Thanks to Michael Seiffert for his support and mentorship during my work on the QUIET project. He taught me a great deal about radiometers, and provided very helpful advice about navigating in the academic world.

That the telescope functioned during this program is thanks to Russ Keeney. His dedication to the telescope and his understanding of its intricacies are awe inspiring. It has been an honor to work with him.

Tony Readhead, my adviser, has been a great teacher and mentor. His enthusiasm for astronomy is infectious, and his obvious love of knowledge in all its forms is inspiring. The support he provided for a graduate student facing the challenges of starting a family while carrying out his research was beyond expectations. It has been a wonderful experience working in his group, and I hope that we will continue to collaborate long into the future.

There are doubtless others who should be named here but have been omitted. My sincere thanks go to all those who have assisted me in this work.

Abstract

Since late 2007, we have regularly monitored over 1100 systematically selected blazars at 15 GHz using the Owens Valley Radio Observatory 40 m radio telescope. The number of sources in the program has grown to nearly 1600, including all the active galactic nuclei associated with *Fermi* Large Area Telescope (LAT) gamma-ray point source detections north of our declination limit of -20° . Here, we describe the first 42 months of this program, including the design and implementation of an automated data reduction pipeline and a MySQL database system for storing the reduced data and intermediate data products. Using the “intrinsic modulation index,” a maximum-likelihood method, we estimate the variability amplitudes for 1413 sources from their radio light curves and compare the properties of physically defined subpopulations of the sample. We find that, among our preselected sample, gamma-ray–loud blazars detected by the LAT are significantly more variable at 15 GHz, attributable to a difference in variability between the gamma-ray–loud and gamma-ray–quiet flat spectrum radio quasars. The BL Lacertae objects in the samples do not show this division in variability amplitudes. In the first two years of our program, a 3σ -significant difference between variability amplitudes for sources at redshift $z \geq 1$ and for sources at $z < 1$ was found. This difference is found no longer to be significant in the full 42-month data set, particularly after we apply an analysis method to account for the effect of cosmological time dilation.

Contents

List of Figures	x
List of Tables	xvi
1 Introduction	1
1.1 Historical Background	3
1.2 Blazar Structure and Emission	4
1.2.1 Structure	5
1.2.2 Emission Processes	5
1.2.3 Jets and Beaming	6
1.2.4 AGN Unification	7
1.2.5 Blazars	8
1.3 The Radio-Gamma Connection	10
1.4 The OVRO 40 m Monitoring Program	11
1.4.1 Impact of OVRO 40 m Data	12
1.4.2 Statistical Considerations	12
1.5 Overview of Thesis	14
2 Telescope, Receiver, and Radiometry	15
2.1 The Hardware	15
2.1.1 The OVRO 40 m Telescope	15
2.1.1.1 Telescope Control Systems	16
2.1.1.2 Mount and Drive System	16
2.1.1.3 Tilt and Temperature Monitoring	17
2.1.1.4 Weather Measurements	17
2.1.2 Optics	18
2.1.2.1 Aperture Efficiency	19
2.1.2.2 Surface Accuracy	21
2.1.2.3 Antenna Gain and Focus	22
2.1.2.4 Beam Map	24

2.1.3	Receiver	28
2.1.3.1	Dicke Switching	30
2.1.3.2	Bandwidth	30
2.1.3.3	Sensitivity	34
2.1.3.4	Gain Fluctuations and $1/f$ Noise	37
2.1.3.5	Calibration Diodes	41
2.1.3.6	Beam Isolation	43
2.1.3.7	Nonlinearity	43
2.2	Radiometry Techniques	46
2.2.1	Calibration and Diagnostic Procedures	46
2.2.1.1	Measuring Receiver and Calibration Diode Noise Temperatures	46
2.2.1.2	Measuring Atmospheric and Ground Pickup	51
2.2.2	Observation Procedures	53
2.2.2.1	Pointing	53
2.2.2.2	Beam Switching and Flux Density Measurements	55
2.2.2.3	Calibration Diode Measurements	58
2.2.2.4	Other Observation Procedures	59
3	Data Reduction Pipeline	60
3.1	Software Tools	62
3.1.1	CMBPROG and the VAX Control System	63
3.1.1.1	VAX Control System	63
3.1.1.2	Overview of CMBPROG	64
3.1.1.3	Retiring CMBPROG	64
3.1.1.4	Interface between CMBPROG and Python	68
3.1.2	Python, Arcreduce, and the MCS Control System	68
3.1.2.1	MCS Control System	68
3.1.2.2	The Arcreduce Python Module	69
3.1.2.3	Reducing Radiometry Procedure Data	74
3.2	Reducing the Data	76
3.2.1	Data Editing and Filtering	78
3.2.1.1	Date Interval Cuts	78
3.2.1.2	Wind, Sun, Moon, and Zenith Angle Cuts	78
3.2.1.3	Pointing and Calibration Failures	79
3.2.1.4	Saturation and Total Power Anomalies	80
3.2.1.5	Measured Uncertainty Cuts	80

3.2.1.6	Switched Difference Cuts	82
3.2.2	Flux Density Calibration	82
3.2.2.1	Relative Calibration	83
3.2.2.2	Long-Term Trends in 3C 286, 3C 274, and DR 21	84
3.2.2.3	Flux Density Calibration	85
3.2.3	Uncertainties in Individual Flux Density Measurements	86
3.2.3.1	Error Model	87
3.2.3.2	Scaling of the Nonthermal Error	88
3.3	Storing and Retrieving the Data	91
3.3.1	Database Design Principles	91
3.3.1.1	Normal Forms	91
3.3.1.2	Table Indexes	92
3.3.2	Representing Sources	93
3.3.3	Storing Observation Data	94
3.3.3.1	FLUX and POINT Procedures	94
3.3.3.2	Flag Tables	96
3.3.4	Managing Data Reduction	97
3.3.5	The Results Database	99
4	Observing Program	100
4.1	Source Selection	100
4.1.1	CGRaBS	101
4.1.2	<i>Fermi</i> -Detected Sources: The 1LAC Sample	102
4.1.3	Calibration Sources	103
4.2	Classifications and Redshifts	104
4.3	Observation Scheduling	109
4.4	Sun and Moon Interference	111
4.5	Confusion	116
4.5.1	Basic Calculation	116
4.5.2	Contaminated FLUX Procedures	117
4.6	Observation Results	118
4.6.1	Observing Efficiency	118
4.6.2	Flux Density Results	122
4.6.3	Future Prospects	122
5	Variability Analysis	126
5.1	Analytical Tools	127

5.1.1	Intrinsic Modulation Index	127
5.1.1.1	Calculating the Intrinsic Modulation Index	129
5.1.2	Properties of the Intrinsic Modulation Index	131
5.1.2.1	Impact of Longer Time Series	136
5.1.2.2	Impact of Data Outliers	138
5.1.3	A Formalism for Population Studies	145
5.2	Null Tests	146
5.2.1	Verifying Data Cuts	147
5.2.2	Physically Insignificant Population Split	148
5.2.3	Galactic Latitude Split	149
5.3	Gamma-Ray Loud versus Quiet Populations	150
5.4	BL Lac Object versus FSRQ Populations	152
5.5	Redshift Trend	156
5.5.1	Cosmological Time Dilation	160
5.5.2	Compensating for Time Dilation	161
5.5.3	Selecting Time Intervals	161
5.5.4	Equal Rest-Frame Time Interval Results	164
5.6	CGRaBS versus 1LAC	165
5.6.1	Flux Density Comparisons	166
5.6.2	High Redshift FSRQ Populations	170
Appendix A	User’s Guide to Arcreduce	173
A.1	High-Level Data Reduction: CalManager	173
A.1.1	CalManager Concepts	173
A.1.1.1	Procedure Class	174
A.1.1.2	Member Class	174
A.1.1.3	Masking and Flagging	175
A.1.1.4	Plotting and Advanced Processing	176
A.1.2	CalManager Tutorial	176
A.1.2.1	Loading Data	176
A.1.2.2	Examining a Procedure	176
A.1.2.3	Working with a Member	177
A.1.2.4	Accessing Data from a Member	178
A.1.2.5	Selecting a Source or Diode	179
A.1.2.6	Applying a Calibration Factor	179
A.1.2.7	Flagging Data	179

A.1.2.8 Example Reduction Script	180
A.1.3 Module Reference	180
A.2 Low-Level Data Processing: ArchiveReader	183
A.2.1 ArchiveReader Class	183
A.2.2 Decoders	185
A.2.3 Output Handlers	189
A.2.4 Procedure Data Structures	189
A.2.5 Exceptions	189
Appendix B Detailed Database Specification	191
B.1 Database Table Diagrams	191
B.2 Domain Table Contents	194
Appendix C Source List	199
Appendix D QUIET	243
D.1 Bias Electronics	243
D.2 Module Protection Circuitry	269
D.3 Housekeeping Measurement Procedures	277
D.4 Receiver Characterization	287
D.5 Low-Noise Preamplifier Design	329
D.5.1 Analysis	329
D.5.1.1 Input Stage	330
D.5.1.2 Differential Stage	330
D.5.1.3 Full Amplifier	332
D.5.2 Prototype Circuit	332
D.5.3 Detector Diode Biasing	333
D.5.4 Conclusions	334
D.6 QUIET 43 GHz Paper	334
References	353

Figures

2.1	Optics and waveguide section block diagram.	19
2.2	Predicted efficiency factor η_p .	21
2.3	Focus curve and relative gain due to focus error.	22
2.4	Example antenna gain curve plotting the relative peak gain as a function of elevation.	24
2.5	Binned switched signal (<i>ant</i> – <i>ref</i>) from 50 min of continuous azimuth scans.	26
2.6	Normalized beam response for the average of the <i>ant</i> and <i>ref</i> beams.	27
2.7	Normalized beam response for both <i>ant</i> (positive) and <i>ref</i> (negative) beams.	27
2.8	Elliptical Gaussian beam fits to the <i>ant</i> (positive) and <i>ref</i> (negative) beams.	28
2.9	Residuals from fits to the beam map data shown in figure 2.7.	29
2.10	Block diagram of the Ku-band receiver.	29
2.11	Photograph of spectrum analyzer sweep of the receiver response.	31
2.12	Piecewise linear approximation to the spectrum analyzer response shown in figure 2.11.	32
2.13	Comparison of the linear and exponential interpolations of the receiver gain.	34
2.14	Simple radiometer model.	35
2.15	Uncalibrated full-rate (500 Hz) Dicke-switched radiometer noise samples.	36
2.16	Power spectral density of 10 min of averaged data, illustrating $1/f$ behavior.	38
2.17	Power spectral density of 10 min of differenced data, illustrating reduced $1/f$ noise.	39
2.18	Power spectral density of about 27 min of noise data.	40
2.19	Change in absolute CAL diode power output versus its case temperature.	42
2.20	One trial of a Y-factor measurement, demonstrating gain compression in the receiver.	44
2.21	Behavior of the compression model.	45
2.22	Receiver temperature measurements.	49
2.23	NOISE diode equivalent noise temperature measurements.	49
2.24	Nonlinearity-corrected NOISE to CAL output ratio measurements.	49
2.25	CAL diode equivalent noise temperature measurements.	50
2.26	Nonlinearity parameter b measurements.	50
2.27	Nonlinearity parameter b_{HC} measurements.	50
2.28	Downward portion of a sky dip (27 April, 2011).	52
2.29	Residual error between the pointing model and the actual requested position.	54

2.30 Pattern of offsets for a POINT2D procedure.	56
2.31 Schematic illustration of the FLUX procedure.	56
3.1 Overview of the data reduction pipeline.	61
3.2 Schematic overview of the MCS control system architecture.	69
3.3 Architecture of the ArchiveReader engine.	73
3.4 Class hierarchy for procedure decoders in the ArchiveReader module.	74
3.5 Illustration of the FLUX procedure decoder.	75
3.6 Illustration of the POINT2D procedure.	77
3.7 Identifying inclement weather using FLUX procedure total power data.	80
3.8 Logarithmic plot of σ_{15}^2 versus S_{15}^2 .	81
3.9 Plot of the switched difference, μ normalized by σ_{15} , versus S_{15} .	83
3.10 Normalized flux densities for 3C 274, DR 21, and 3C 286 after outlier removal.	84
3.11 Normalized flux densities for 3C 274, DR 21, and 3C 286 after dividing by the spline fit.	85
3.12 Comparison of residual standard deviation with ϵ -only error model.	88
3.13 Example of the error scale factor correction using data for J1044+5322.	90
3.14 Histogram of the change in error scale factors for CGRaBS.	90
3.15 Diagram illustrating the database tables used for storing source data.	93
3.16 Diagram illustrating the database tables used for storing observation data.	95
3.17 Diagram illustrating the database tables used for storing flag types and parameters.	96
3.18 Diagram illustrating the database tables used for storing date interval flags.	97
3.19 Diagram illustrating the database tables used for storing reduction data.	98
4.1 Positions of the CGRaBS sources in our program in equatorial coordinates.	101
4.2 Positions of the 1LAC sources in our program in equatorial coordinates.	103
4.3 Optical classifications for the CGRaBS sample.	105
4.4 Optical classifications for the 1LAC sample.	106
4.5 Histograms of redshifts for CGRaBS, the FSRQ subset, and the BL Lac subset.	106
4.6 Histograms of redshifts for 1LAC, the FSRQ subset, and the BL Lac subset.	107
4.7 Venn diagram showing the relationship between the CGRaBS and 1LAC samples.	109
4.8 Example of an observation region.	111
4.9 Source-nulled flux (S_{null}) as a function of solar elongation.	112
4.10 Detail of figure 4.9, showing features at small solar elongation.	113
4.11 Evidence of contamination in the total power signal at small solar elongations.	114
4.12 Detail of figure 4.11 with bins of $\sim 0.25^\circ$.	115
4.13 Reference field coverage during the full data set for four sources.	119
4.14 Histogram of per-source observing efficiency for CGRaBS sources.	120

4.15 Histogram of per-source observing efficiency for 1LAC sources.	120
4.16 Weekly observation counts for each year of observations.	121
4.17 Histograms of the distributions of per-source median flux density in the CGRaBS sample.	123
4.18 Histograms of the distributions of per-source median flux density in the 1LAC sample.	124
5.1 Likelihood parameter space, showing 1σ , 2σ , and 3σ contours for blazar J1243–0218.	130
5.2 Marginalized likelihood $\mathcal{L}(m)$ for J1243–0218.	130
5.3 Maximum-likelihood Gaussian model for the flux density distribution of J1243–0218.	131
5.4 Histogram of measurements for J0237+3022, demonstrating a bimodal distribution.	132
5.5 Intrinsic modulation index versus average flux density.	133
5.6 Intrinsic modulation index versus “raw” modulation index.	135
5.7 Histogram of intrinsic modulation indices for bright CGRaBS blazars.	136
5.8 Scatter plot comparing 42-month and two-year modulation indices.	137
5.9 Histogram of the intrinsic modulation indices for the two-year and 42-month data sets.	138
5.10 Change in intrinsic modulation indices between the two-year and 42-month data sets.	139
5.11 Light curves for sources with the most significant changes in intrinsic modulation index.	140
5.12 Effect of an extreme outlier data point on the intrinsic modulation index.	141
5.13 Histogram of intrinsic modulation indices with and without an extreme outlier.	142
5.14 Effect of an extreme outlier versus true intrinsic modulation index.	142
5.15 Effect of an extreme outlier versus average flux density.	143
5.16 Verification that the data cuts described in section 5.1.2 are correctly implemented.	147
5.17 Null test of population comparison method using two-year data.	148
5.18 Null test of population comparison method using 42-month data.	149
5.19 Histograms comparing intrinsic modulation indices for the 42-month null test.	150
5.20 Comparison of high and low galactic latitude bright CGRaBS populations.	151
5.21 Comparison of gamma-ray–loud and gamma-ray–quiet CGRaBS using two-year data.	151
5.22 Comparison of gamma-ray–loud and gamma-ray–quiet CGRaBS using 42-month data.	152
5.23 Intrinsic modulation indices of gamma-ray–loud and gamma-ray–quiet CGRaBS.	153
5.24 Comparison of CGRaBS BL Lac and FSRQ populations using two-year data.	154
5.25 Comparison of CGRaBS BL Lac and FSRQ populations using 42-month data.	154
5.26 Intrinsic modulation indices of CGRaBS BL Lac and FSRQ sources.	155
5.27 Comparison of 1LAC BL Lac and FSRQ populations using 42-month data.	155
5.28 Intrinsic modulation indices of 1LAC BL Lac and FSRQ sources.	156
5.29 Mean \bar{m} versus z for bright CGRaBS FSRQs, comparing two-year and 42-month data.	157
5.30 Comparison of high- and low-redshift CGRaBS FSRQs using two-year data.	157
5.31 Comparison of high- and low-redshift CGRaBS FSRQs using 42-month data.	158

5.32 Comparison of high- and low-redshift 1LAC FSRQ populations using 42-month data.	158
5.33 Intrinsic modulation indices for high- and low-redshift CGRaBS sources.	159
5.34 Intrinsic modulation indices for high- and low-redshift 1LAC sources.	159
5.35 Observer time interval for each source plotted versus redshift.	162
5.36 Number of data points in the equal- Δt_{rest} data sample for each source.	163
5.37 Histogram of redshifts for the 1LAC FSRQs with known $z < 3.0$	163
5.38 Comparison of high- and low-redshift 1LAC FSRQs with equal rest-frame intervals.	164
5.39 Comparison of CGRaBS and 1LAC BL Lac populations.	166
5.40 Comparison of CGRaBS and 1LAC FSRQ populations.	167
5.41 Histograms of S_0 comparing overall CGRaBS and 1LAC populations.	167
5.42 Histograms of S_0 comparing FSRQ and BL Lac subsamples of CGRaBS and 1LAC samples.	168
5.43 Histograms of S_0 comparing CGRaBS and 1LAC subsamples of FSRQ and BL Lac samples.	169
5.44 OVRO 40 m 15 GHz average flux density versus archival 8 GHz flux density.	170
5.45 Histograms of intrinsic modulation indices for CGRaBS FSRQs at $z > 1.5$	171
5.46 Comparison between high-redshift CGRaBS FSRQ populations in and not in 1LAC.	171
B.1 Diagram illustrating the database tables used for storing wind speed data.	191
B.2 Diagram illustrating the database tables used for storing epoch definitions.	192
B.3 Diagram illustrating the database tables used for storing error scale factors.	192
B.4 Diagram illustrating the database tables used for storing focus model data.	192
B.5 Diagram illustrating the database tables used for storing gain curves.	193
B.6 Diagram illustrating the database tables used for storing polynomial definitions.	193
B.7 Diagram illustrating the database tables used for storing calibration spline definitions.	193
D.1 Figure 1: Mechanical drawing of board outline and keep-outs.	256
D.2 Figure 1: Schematic of gate protection to be installed on MAB.	272
D.3 Figure 2: Schematic of drain protection to be installed on MAB.	272
D.4 Figure 3: Schematic of phase switch protection to be installed on MAB.	272
D.5 Figure 4: Schematic of gate protection on the MMIC bias card.	273
D.6 Figure 5: Schematic of drain protection circuit on the MMIC bias card.	273
D.7 Figure 6: Schematic of protection circuit on the phase switch bias card.	273
D.8 Figure 1: Housekeeping analog optoisolator voltage transfer curve.	280
D.9 Figure 2: Schematic of a single gate control and housekeeping circuit.	281
D.10 Figure 3: Gate measurement errors for a W-band single-board MAB with no module . . .	283
D.11 Figure 4: Simplified drain schematic	284
D.12 Figure 5: Drain voltage and current estimate errors versus actual drain voltage	285
D.13 Figure 6: Same data from Figure 5, now plotted versus the housekeeping drain voltage . .	286

D.14 Figure 1: Rising edge of phase switch clock and falling voltage on phase switch diode.	290
D.15 Figure 2: Falling edge of phase switch clock and rising voltage on phase switch diode.	291
D.16 Figure 3: Gain curve for D1.	293
D.17 Figure 4: Gain curve for D4.	293
D.18 Figure 5: Channel A data acquisition system noise baseline.	294
D.19 Figure 6: Channel B data acquisition system noise baseline.	294
D.20 Figure 7: A-B difference noise spectrum.	295
D.21 Figure 8: Comparison of time series data from D1 in the two phase states.	296
D.22 Figure 9: Noise spectrum of D1 “plus” state with no differencing.	296
D.23 Figure 10: Noise spectrum of D4 “plus” state with no differencing.	297
D.24 Figure 11: Single-difference noise spectrum from D1.	297
D.25 Figure 12: Single-difference noise spectrum from D4.	298
D.26 Figure 13: Single-difference noise spectrum of D1 “plus” minus D4 “plus.”	298
D.27 Figure 14: Single-difference noise spectrum of D1 “plus” minus D4 “minus.”	299
D.28 Figure 15: Single-difference noise spectrum of D1 “minus” minus D4 “plus.”	299
D.29 Figure 16: Single-difference noise spectrum of D1 “minus” minus D4 “minus.”	300
D.30 Figure 17: Double-difference noise spectrum between D1 and D4.	300
D.31 Figure 18: Weighted D1 single-difference noise spectrum.	301
D.32 Figure 19: Weighted double-difference noise spectrum between D1 and D4.	302
D.33 Figure 1: Alignment of blanking period with actual phase switch transition.	304
D.34 Figure 2: D1 “plus” phase state spectrum before and after the blanking fix.	304
D.35 Figure 3: Comparison of equal-length “before” and “after” noise spectra.	305
D.36 Figure 4: Unweighted single-difference data from D1 for “before” and “after” data.	305
D.37 Figure 5: Undifferenced D1 “plus” state spectrum.	306
D.38 Figure 6: D1 unweighted single difference spectrum.	307
D.39 Figure 7: D1 weighted single difference spectrum.	307
D.40 Figure 8: D4 unweighted single difference spectrum.	308
D.41 Figure 9: D4 weighted single difference spectrum.	308
D.42 Figure 10: Unweighted double difference spectrum.	309
D.43 Figure 11: Doubly-weighted double difference spectrum.	309
D.44 Figure 12: Undifferenced data plotted separately for each diode and phase switch state.	310
D.45 Figure 13: D1 unweighted single difference spectrum.	311
D.46 Figure 14: D1 weighted single difference spectrum.	311
D.47 Figure 15: D4 unweighted single difference spectrum.	312
D.48 Figure 16: D4 weighted single difference spectrum.	312
D.49 Figure 17: Unweighted double difference spectrum.	313

D.50 Figure 18: Doubly-weighted double difference spectrum.	313
D.51 Figure 1: Schematic of the RF portion of the test apparatus.	316
D.52 Figure 2: Typical spectrum of test set noise.	316
D.53 Figure 3: Typical spectrum from a 5000-second (1.4 hour) data set.	318
D.54 Figure 4: Gain fluctuations as a function of MMIC drain voltage.	318
D.55 Figure 5: Gain fluctuations as a function of MMIC drain current.	319
D.56 Figure 6: Gain fluctuations as a function of DC detected voltage.	319
D.57 Figure 7: Spectral density at 1 Hz as a function of MMIC drain voltage.	320
D.58 Figure 8: Spectral density at 1 Hz as a function of MMIC drain current.	320
D.59 Figure 1: RF test set schematic for the uncorrelated MMIC tests.	323
D.60 Figure 2: Simulated cross-spectrum of two independent $1/f$ -noise series.	324
D.61 Figure 3: Power and cross-spectra of fully independent input signals.	324
D.62 Figure 4: High-frequency power and cross-spectra of independent input signals.	325
D.63 Figure 5: Histogram of the cross-spectrum data from Figure 4.	326
D.64 Figure 6: Histogram of power spectral density data.	326
D.65 Figure 7: Probability density function of $\text{sign}(x)\sqrt{ x }$ for a Gaussian random variable x	327
D.66 Full preamp schematic.	329
D.67 Schematic of input amplifier stage.	330
D.68 Schematic of differential amplifier stage.	331
D.69 One possible scheme for biasing the detector diode and generating a DC offset signal.	333
D.70 Fig. 1— Overview of the QUIET instrument.	336
D.71 Fig. 2— The CMB and Galactic patches, in equatorial coordinates.	337
D.72 Fig. 3— Polarimeter responses from the central feed horn to the polarization of Tau A.	338
D.73 Fig. 4— Map of the polarization of the Moon from one detector diode.	339
D.74 Fig. 5— Polarization beam profile and beam window function.	340
D.75 Fig. 6— EE and BB power spectra for the patch CMB-1 null test.	344
D.76 Fig. 7— Power-spectra differences between the final data selection and earlier iterations. . . .	345
D.77 Fig. 8— Null-suite statistics.	345
D.78 Fig. 9— EE, BB, and EB power spectra from each QUIET pipeline, all four patches combined.	346
D.79 Fig. 10— Maps of patch CMB-1 in Galactic coordinates.	347
D.80 Fig. 11— EE and BB results.	348
D.81 Fig. 12— CMB power spectra are shown for each patch individually.	349
D.82 Fig. 13— CMB temperature map and power spectra.	349
D.83 Fig. 14— Systematic uncertainty estimates for EE, BB, and EB power spectra.	350

Tables

2.1	List of thermometers instrumenting the 40 m telescope	17
2.2	Aperture efficiency measurement results	20
2.3	Focus curve values plotted in the left-hand panel of figure 2.3	23
2.4	Polynomial coefficients for the focus models (before and after April 2010)	23
2.5	Polynomial coefficients of the focus miss curve (before and after April 2010)	23
2.6	Gain curve polynomial coefficients (before and after April 2010)	24
2.7	Properties of a few point sources suitable for beam mapping	25
2.8	Results of fitting Gaussian components to the beam center scan in figure 2.5	25
2.9	Elliptical Gaussian beam fit parameters	28
2.10	Segment endpoints for the piecewise linear approximation to the measured receiver gain . .	32
2.11	Calculation of receiver sensitivity and comparison with the radiometer equation	36
2.12	Results of a stability test of CAL diode output versus diode case temperature	42
2.13	Results of a stability test of NOISE diode output versus diode case temperature	42
3.1	Flux density bins used for fitting the measured uncertainty filter parameters	81
3.2	Calibrator spline epochs	85
3.3	Flux density calibration epochs	86
3.4	Error model parameters	87
4.1	Source counts in the CGRaBS and <i>Fermi</i> 1LAC samples	102
4.2	Usage of calibration sources in this program	103
4.3	Contamination estimates at various flux density limits, S_c	118
5.1	Fraction of sources determined to be affected by an extreme low outlier	144
A.1	List of CalManager procedures	174
A.2	Descriptions of the CalManager procedure members	175
A.3	Flag values supported by CalManager	180
B.1	Contents of the Active table	194
B.2	Contents of the Catalog table	194

B.3	Contents of the Classification table	194
B.4	Contents of the Reference table	195
B.5	Contents of the FluxType table	195
B.6	Contents of the ReductionParameterName table	195
B.7	Contents of the ReductionType table	195
B.8	Contents of the ParameterDataType table	196
B.9	Contents of the DataSource table	196
B.10	Contents of the FlagType table	196
B.11	Contents of the FlaggedDateType table	197
B.12	Contents of the EpochType table	197
B.13	Contents of the FocusModelTerm table	197
B.14	Contents of the SplineDatumType table	197
B.15	Contents of the WeatherDataSource table	198
C.1	List of sources in the monitoring program	199
D.1	Table 1: MMIC bias card design/construction schedule	245
D.2	Table 2: Summary of interface signal counts for the MMIC bias card	247
D.3	Table 3: 90 GHz module bias control signals and DAC channel assignments	248
D.4	Table 4: 40 GHz and 90 GHz module gate bias requirements	248
D.5	Table 5: 40 GHz and 90 GHz module drain bias requirements	249
D.6	Table 6: MMIC bias card output capabilities	249
D.7	Table 7: Bias output noise requirements	250
D.8	Table 8: DAC interface signals	250
D.9	Table 9: DAC control word ordering	250
D.10	Table 10: DAC control word format	251
D.11	Table 11: Time required to set DAC control words at various serial clock rates	251
D.12	Table 12: Receiver module multiplexer sub-addresses	252
D.13	Table 13: MMIC bias monitor signals for each receiver module	253
D.14	Table 14: Main power supplies for each MAB	253
D.15	Table 15: Optoisolator power supplies for each MMIC bias card	254
D.16	Table 16: FPC connection requirements	255
D.17	Table 17: Per-card overhead power dissipation estimates	257
D.18	Table 1: Phase switch bias card design/construction schedule	259
D.19	Table 2: Summary of interface signal counts for the phase switch bias card	260
D.20	Table 3: Phase switch bias control signals	261
D.21	Table 4: Phase switch bias requirements	261

D.22 Table 5: Phase switch bias card output capabilities	261
D.23 Table 6: DAC interface signals	262
D.24 Table 7: DAC interface signals	263
D.25 Table 8: DAC control word format	263
D.26 Table 9: PCLK truth table	264
D.27 Table 10: Receiver module multiplexer sub-addresses	264
D.28 Table 11: Phase switch bias monitor signals for each receiver module	265
D.29 Table 12: Main power supplies for each phase switch bias card	265
D.30 Table 13: Optoisolator power supplies for each phase switch bias card	266
D.31 Table 14: FPC connection requirements	266
D.32 Table 1: Gate circuit resistor values for W- and Q-band	281
D.33 Table 2: Drain circuit values for both W- and Q-bands	282
D.34 Table 1: Noise-effective bandwidths	292
D.35 Table 2: Data for noise-effective bandwidth calculation	292
D.36 Table 1. Patch locations and integration times	338
D.37 Table 2. Regular calibration observations	338
D.38 Table 3. Total hours observed and data-selection efficiencies	342
D.39 Table 4. Null suite probability to exceed by patch	345
D.40 Table 5. CMB-spectra band powers from QUIET Q-band data	347
D.41 Table 6. Band and cross powers for $\ell = 25\text{--}75$	349